

## IS THE TAURUS B213 REGION A TRUE FILAMENT?: OBSERVATIONS OF MULTIPLE CYANOACETYLENE TRANSITIONS

DI LI<sup>1,2,3</sup>, PAUL F. GOLDSMITH<sup>3</sup>

*Draft version February 7, 2022*

### ABSTRACT

We have obtained spectra of the J=2-1 and J=10-9 transitions of cyanoacetylene (HC<sub>3</sub>N) toward a collection of positions in the most prominent filament, B213, in the Taurus molecular cloud. The analysis of the excitation conditions of these transitions reveals an average gas H<sub>2</sub> volume density of  $(1.8 \pm 0.7) \times 10^4 \text{ cm}^{-3}$ . Based on column density derived from 2MASS and this volume density, the line of sight dimension of the high density portion of B213 is found to be  $\simeq 0.12 \text{ pc}$ , which is comparable to the smaller projected dimension and much smaller than the elongated dimension of B213 ( $\sim 2.4 \text{ pc}$ ). B213 is thus likely a true cylinder-like filament rather than a sheet seen edge-on. The line width and velocity gradient seen in HC<sub>3</sub>N are also consistent with Taurus B213 being a self-gravitating filament in the early stage of either fragmentation and/or collapse.

*Subject headings:* ISM:structure – ISM: individual objects:Taurus–ISM:molecules–  
Techniques:spectroscopic

### 1. INTRODUCTION

The advent of telescopes with large format imaging arrays, such as Herschel and JCMT, makes possible maps of star forming regions with large spatial dynamic ranges. It has become apparent in such images in both gas (Narayanan et al. 2008) and dust emission (Men'shchikov et al. 2010; Arzoumanian et al. 2011) that, when properly sampled, molecular gas clouds exhibit filamentary structures on many spatial scales. This confirms the morphology that had been identified earlier in studies of visual extinction (Schneider & Elmegreen 1979). The origin of such elongated structures is unclear. A filament as a projected two dimensional structure, can be consistent with different theories. In particular, models suggest that gravitationally bound cigar-like clouds will collapse to become spindles, while pancake-like clouds will continue to flatten under the influence of their self-gravity to become sheet-like structures (Lin et al. 1965; McKee & Ostriker 2007). In shock-induced molecular cloud formation models, the region around shock front will also be flattened (Vázquez-Semadeni et al. 2006).

To distinguish a true filamentary (cylinder like) structure from a sheet seen projected essentially edge-on, we have sought to obtain the line of sight dimension of a prominent dense filament in Taurus, B213 (Fig. 1). Taurus is one of the closest star forming regions. The portion of Taurus molecular cloud that contains B213 filament has been covered by a rich collection of surveys at optical through radio wavelengths (Goldsmith et al. 2008; Rebull et al. 2010). For this study, we have obtained data along “cuts” in the direction orthogonal to the elongation of the filament, in order to evaluate the variation of the excitation conditions in the filament, and to determine its volume density from which the line of

sight dimension can be determined.

The column density of the molecular gas can be determined by optically thin tracers including gas and dust. Goldsmith et al. (2008) presented a column density map of the whole Taurus region through analysis combining <sup>13</sup>CO 1-0 and <sup>12</sup>CO 1-0 transitions. There have been only a few previous attempts to determine the volume density of gas in Taurus. The first of these was by Avery et al. (1982), who observed a few positions towards TMC-1, a well-known high-density region. Avery et al. (1982) obtained five transitions (J=4-3, 5-4, 9-8, 10-9, and 11-10) of cyanoacetylene (HC<sub>3</sub>N) at millimeter wavelengths. Their excitation analysis found a halo component having density  $8 \times 10^3 \text{ cm}^{-3}$  and a core having a density  $6 \times 10^4 \text{ cm}^{-3}$ . TMC-1 is part of the observed ring-like structure, but is not really a filament as are many other structures seen in Taurus. Schloerb, Snell & Young (1983) studied the same region in three transitions of HC<sub>3</sub>N, and found a single density  $10^5 \text{ cm}^{-3}$  to fit their data satisfactorily. If the  $\sim 1$  to 2 arcminute telescope beams are filled by gas at these relatively high densities, the line of sight dimension must be quite small, about 0.1pc, in order to be consistent with the column density. Considering the molecular ring to be a tube of circular form, the diameter of the tube is no more than 0.4 pc. This does not give clear evidence for any extreme geometry. Pratap et al. (1997) derived the density for positions in TMC1 based on the J=4-3, 10-9, and 12-11 transitions of HC<sub>3</sub>N. The range of densities are generally consistent with the core value from Avery et al. (1992), but Pratap et al. did not observe TMC1C. Onishi et al. (2002) identified a large number of cores in Taurus using H<sup>13</sup>CO<sup>+</sup> J = 1-0. The detection of this spectral line is generally suggestive of high densities,  $10^5 \text{ cm}^{-3}$ , but since only a single transition of this species was observed, the density could not be directly determined. Stepnik et al. (2003) made a cut across a dense filament in Taurus at multiple wavelengths between 200 to 400 microns. Their model (which has large uncertainties) suggests a peak density  $\sim 6 \times 10^4 \text{ cm}^{-3}$ , which suggests a true filamentary geometry.

<sup>1</sup> National Astronomical Observatories, Chinese Academy of Sciences, Chaoyang District, Datun Rd, A20, Beijing 100012, China, email: dili@nao.ac.cn

<sup>2</sup> Space Science Institute, Boulder, CO, USA

<sup>3</sup> Jet Propulsion Laboratory, California Institute of Technology, Pasadena, CA, USA

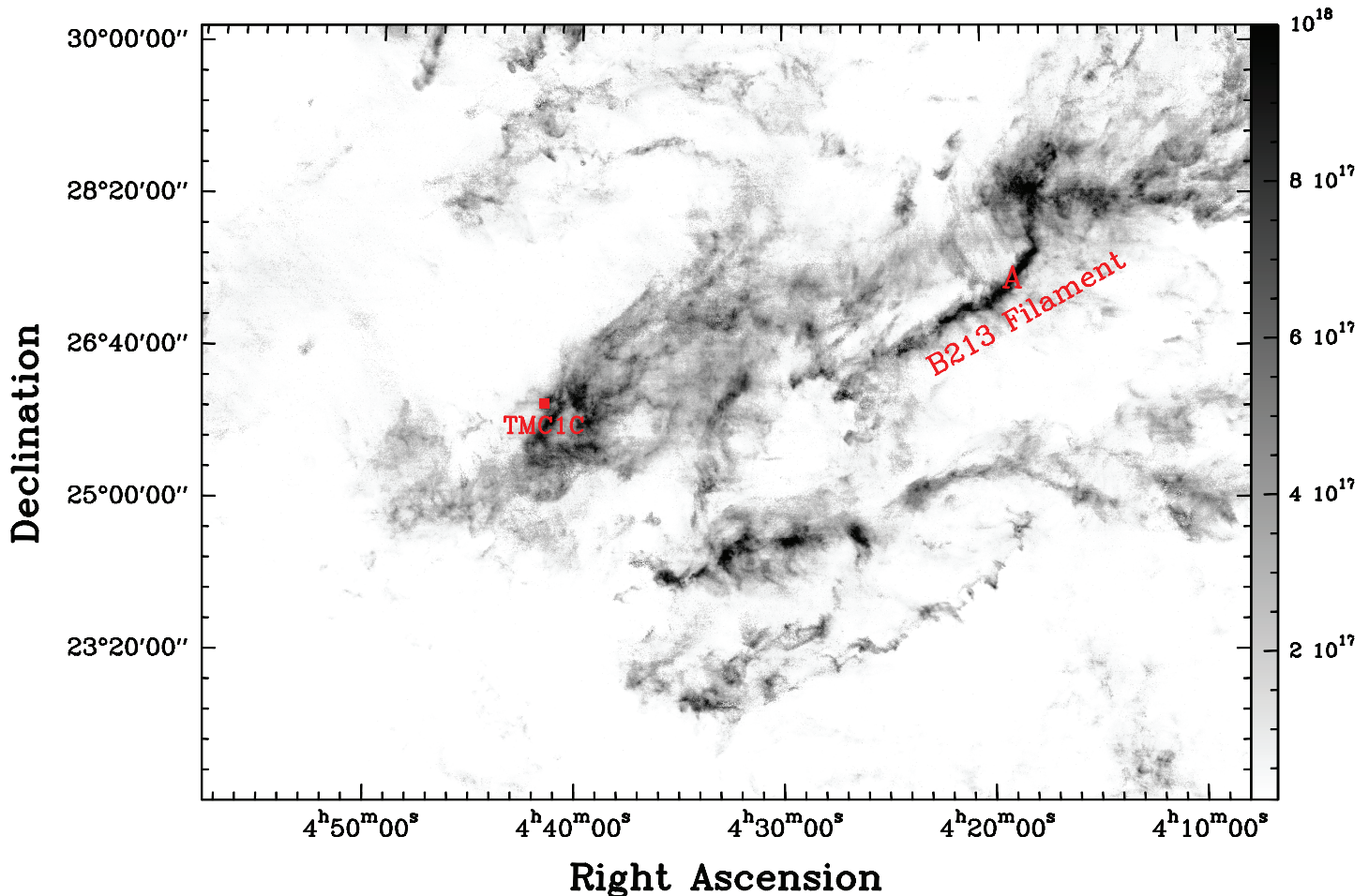


FIG. 1.—  $^{12}\text{CO}$  column density map of the Taurus molecular cloud containing B213 filament. The coordinates in this and subsequent figures are J(2000). The red letter "A" indicates the location of  $\text{HC}_3\text{N}$  measurements and is the same as the position A in Fig. 4. The red square indicates TMC1C.

In this study, we focus on using J=2-1 and J=10-9 transitions of  $\text{HC}_3\text{N}$  as a density probe, which has the following advantages. The excitation of these spectral lines is sensitive to the volume density in likely range of this quantity of relevance to Taurus. When the 2-1 transition at 18.2 GHz is observed with the 100 meter Green Bank Telescope (GBT), the resulting FWHM beam size is close to  $40''$ , which is similar to the  $69''$  beam of the 12 meter telescope of the Arizona Radio Observatory (ARO) at the 90.979 GHz frequency of the 10-9 transition.

## 2. OBSERVATIONS

At the Green Bank Telescope (GBT), we obtained data on the  $\text{HC}_3\text{N}$  J=2-1 transition toward positions across several filaments and TMC1C in the Taurus molecular cloud. The data were taken in two runs on 12 and 25 February 2009. The observations were carried out in frequency switching mode with a frequency throw of 3 MHz, which is relatively small compared to the total bandwidth of 50 MHz. The total number of channels is 8096 with a velocity resolution of 0.1 km/s. The resulting spectra have flat baselines and the emission is easily recovered through folding procedures (Fig. 2). The intensity calibration was done following the procedure in the GBTidl manual written by J. Braatz. The calibration requires the knowledge of atmospheric zenith optical depth at 18

GHz, which was provided by the GBT weather forecast tool to be 0.0183 for 12 February and 0.035 for 25 February. The resulting antenna temperatures were further scaled to main beam temperatures by using a main beam efficiency of 0.88 (provided by GBTidl).

At the Arizona Radio Observatory 12m telescope (ARO), we observed the  $\text{HC}_3\text{N}$  10-9 and 12-11 transitions toward the same set of filaments. Only the 10-9 transition was detected and only in positions across the B213 filament. Between 2009 and 2010, we also carried out three runs to map out the spatial extent of the 10-9 emission in B213. The  $\text{HC}_3\text{N}$  data were taken in position switching mode at ARO. A simple correction was then applied to scale the data to main beam antenna temperature using the main beam efficiency of 0.87 at 91 GHz from the ARO online manual. As seen in Fig. 3, the hyperfine components of the 10-9 transitions are not resolved.

## 3. RESULTS OF DATA ANALYSIS

In all observing runs at both GBT and ARO, we observed TMC1C regularly to check the system and use it as a secondary flux calibrator. The analysis of these spectra are discussed in the following subsection using TMC1C as an example. The scientific analysis in §4 and §5 will focus on observations of B213.

### 3.1. TMC1C

TMC1C exhibits strong  $\text{HC}_3\text{N}$   $J=2-1$  emission with peak main beam antenna temperature of the  $F=3-2$  component being over 3 K. We did not detect the 2-1 line toward other targets in Taurus except for the B213 filament. This is a reflection of a much lower abundance of  $\text{HC}_3\text{N}$  compared to that of TMC1C. The chemical differentiation in the Taurus region, although an interesting topic by itself, is beyond the scope of this paper. The dense core TMC1C has been known to exhibit strong emission in transitions of carbon chain molecules. We observed this source both as a relative intensity calibrator and as a test of our analysis procedures.

The  $\text{HC}_3\text{N}$  2-1 transition has 6 hyperfine components, five of which can be clearly seen in our spectrum of TMC1C. We fit all hyperfine components using the “hfs” fitting method in the GILDAS CLASS package (<http://www.iram.fr/IRAMFR/GILDAS>). The basic assumptions are a single line width for all hyperfine components and no blending, both of which are reasonable for TMC1C. The fitted line characteristics are given in Table 2. The fitted peak optical depth is 0.47. This is a modest opacity, estimated with the reasonable assumption that excitation temperature of all hyperfine components are the same.

The optical depth of the  $F=3-2$  hyperfine component, and the corrected peak antenna temperature of the  $F=3-2$  component are given in columns 7 and 5 of Table 2. The integrated intensity of each hyperfine component is corrected for its own optical depth, and the corrected integrated intensities for the  $J=2-1$  transition are given in column 6 of Table 2.

### 3.2. The B213 Filament

The data toward B213 were taken in the same setup as used for TMC1C. We observed a number of positions, which are indicated in Fig. 4, which shows all observed lines of sight toward B213 in both the  $J=2-1$  and the  $J=10-9$  transition. We have detected both 10-9 and 2-1 transitions in a total of 5 adjacent positions. The coordinates for these positions are given in Table 1. The extent of emission is delineated on three sides by non-detections and is well constrained within the ridge. There are two velocity components of  $\text{HC}_3\text{N}$  in this region, which correspond to components seen in  $^{13}\text{CO}$ . The main component is at around 5.7 km/s, while the second component peaks at around 6.8 km/s. In the direction orthogonal to the elongation of the filament, the size of  $\text{HC}_3\text{N}$  emission is between 2 and 3 arcminutes. The analysis of the density structure will focus on these 5 positions.

These spectra are complicated by the fact that there are two velocity components in this filament. The displacement of these two components is about 1 km/s, which makes them blended in tracers with larger velocity dispersion, such as CO and its isotopologues. Due to the narrowness of  $\text{HC}_3\text{N}$  lines, the two velocity components are clearly resolved. In Fig. 5, we show the  $J=10-9$  line at position A. A two component Gaussian fit reveals the peak velocities to be 5.6 and 6.7 km/s. The peak temperatures are 0.20 and 0.16 K, and the FWHM 0.28 and 0.20 km/s, respectively.

The  $J=2-1$  line of  $\text{HC}_3\text{N}$  in B213 contains both hyperfine and multiple velocity components. In Fig. 6 we show

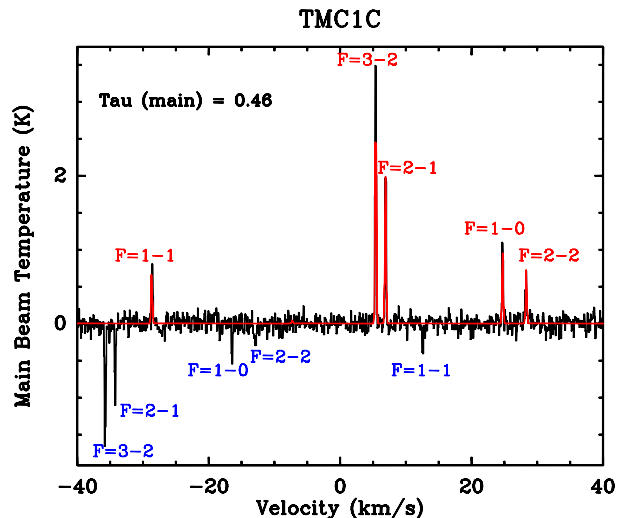


FIG. 2.— Spectrum of the  $\text{HC}_3\text{N}$   $J=2-1$  line toward TMC1C. A double-frequency-switching mode was employed to obtain these data. The negative peaks (blue labels) are a consequence of the folding process used to analyze a frequency switched spectrum. The negative  $F=2-2$ ,  $F=1-0$ ,  $F=2-1$ , and  $F=3-2$  components are a result of a shift to higher frequency, while the  $F=1-1$  negative component is due to a shift to lower frequency. The intensity scale is the main beam antenna temperature, as described in the text. The hyperfine fit to the spectrum gives peak antenna temperature (corrected for optical depth) of the  $F=3-2$  component to be 5.3 K,  $V_{lsr}$  equal to 5.4 km/s, and FWHM equal to 0.21 km/s.

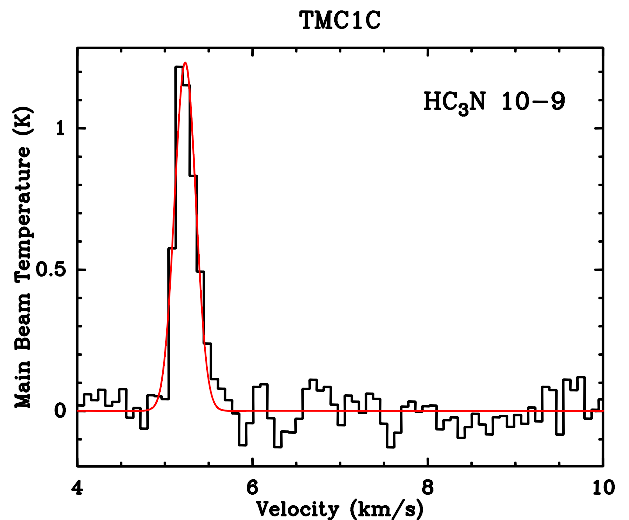


FIG. 3.— Spectrum of the  $\text{HC}_3\text{N}$   $J=10-9$  line toward TMC1C. A single Gaussian fit gives  $V_{lsr}$  equal to 5.2 km/s, FWHM equal to 0.29 km/s, and integrated area equal to 0.38 K km/s. The peak of the fitted Gaussian is 1.23 K.

the  $J=2-1$  spectrum of position A, in which a total of four peaks are visible due to the two stronger hyperfine components for each of the two velocity components, on the same velocity range as that of Fig. 5. The two observed hyperfine components of the 2-1 line are separated by about 1.5 km/s. We have performed hyperfine fits for

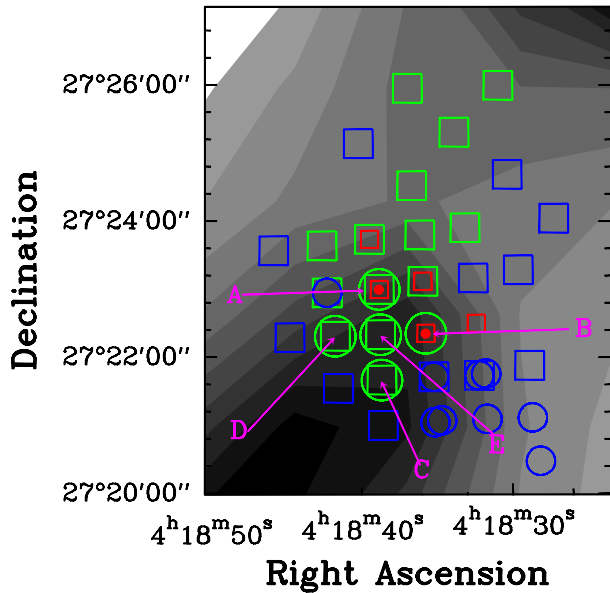


FIG. 4.— A summary of our pointings and  $\text{HC}_3\text{N}$  detections. The underlying image is of magnitude of 2MASS extinction (Pineda et al. 2010). The blue symbols represent non-detections, the green symbols represent detection of the 5.6 km/s component, and the red symbols represent detection the 6.7 km/s component (see text). The circles denote the J=2-1 transition and the squares denote the J=10-9 transition. The combination of shape and color represents whether emission in a particular velocity component is detected or not in a particular transition.

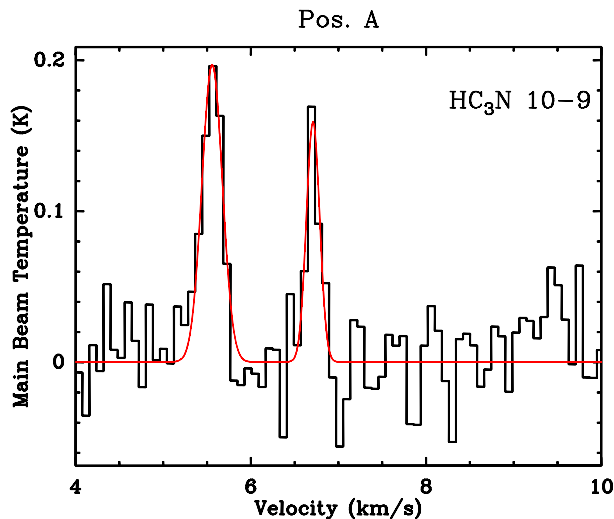


FIG. 5.— Spectrum of the  $\text{HC}_3\text{N}$  J=10-9 line toward position A in the B213 filament. The red line is the result of a two velocity component Gaussian fit with parameters given in the text and in Table 2.

each of the velocity components to derive their optical depths. The lower velocity component is found to have a peak optical depth of 0.48, similar to that of TMC1C. The higher velocity component is found to be optically thin. The total column densities of TMC1C and B213 traced by 2MASS extinction (Pineda et al. 2010) are similar. The difference in line strength by a factor of 10 or more is thus attributable to a much higher  $\text{HC}_3\text{N}$  abun-

TABLE 1  
SOURCE LIST

Source	Right Ascension (J2000)	Declination (J2000)
TMC1C	04:41:38.82	26:00:42.3
B213 A	04:18:38.45	27:23:00.6
B213 B	04:18:35.45	27:22:20.6
B213 C	04:18:38.45	27:21:40.6
B213 D	04:18:41.45	27:22:20.6
B213 E	04:18:38.45	27:22:20.6

dance in TMC1C. This chemical variation is not a focus of this paper and does not affect the excitation analysis and the derived volume density in the following sections.

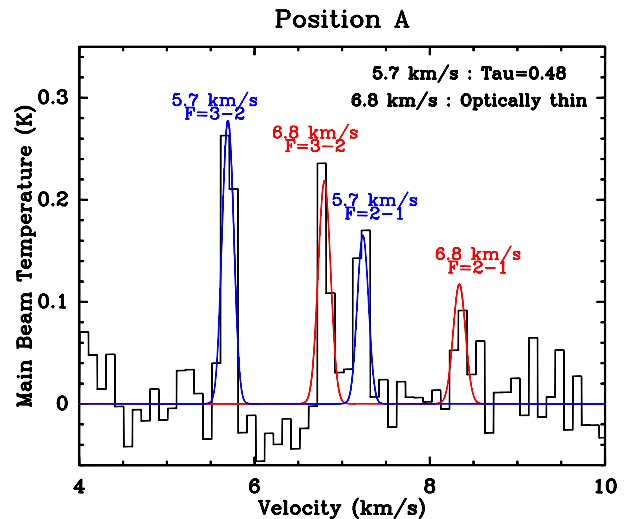


FIG. 6.— Spectrum of the  $\text{HC}_3\text{N}$  J=2-1 line toward position A in the B213 filament. The velocity scale is referenced to the strongest (F=3-2) hyperfine component, which shows two velocity components, at 5.7 km/s and 6.8 km/s. The peaks at 7.3 and 8.5 km/s are due to the F = 2-1 hyperfine component. The blue and red lines represent the hyperfine fits including two velocity components.

#### 4. DENSITY DETERMINATION THROUGH EXCITATION ANALYSIS OF $\text{HC}_3\text{N}$ TRANSITIONS

Filaments can be defined as elongated structures in two spatial dimensions observed in images of both dust and gas. Such structures are found to be prevalent in star forming regions. The physics of filament formation and its implication for star formation hinges on the three dimensional geometry of such structures. The essentially unknown line of sight (los) dimension of structures that have very unequal dimensions in the plane of the sky (pos) is critical for determining whether the structures are filaments if  $d_{los}$  is comparable to the smaller pos dimension or sheets viewed edge on if  $d_{los}$  is comparable to the larger pos dimension. To determine  $d_{los}$ , one need both volume density and column density. In this section, we derive the volume density based on excitation analysis of  $\text{HC}_3\text{N}$  transitions.

In order to compare our data with statistical equilibrium calculations of the excitation of the observed  $\text{HC}_3\text{N}$  lines, we correct the integrated intensity of the  $J=2-1$  line by the optical depth derived through fitting the hyperfine components. The integrated intensity of each hyperfine component is corrected for its own optical depth. The line ratio in Table 2 refers to the ratio between the total  $J=2-1$  integrated intensity and the integrated intensity of the  $J=10-9$  line. This line ratio is what is modeled by the intensities given by our radiative transfer calculations in which the hyperfine components are not explicitly considered.

The situation for analyzing collisional excitation of cyanoacetylene in order to determine the local density has improved significantly of late. Green and Chapman (1978) carried out close-coupling calculations of rotational excitation in collisions with helium representing molecular hydrogen in its lowest,  $J = 0$ , spherically symmetric state. These calculations were used in some of the works cited above. The first calculations that treated ortho- and para-  $\text{H}_2$  as distinct species were carried out by Wernli et al. (2007a). The improvements in the calculation of the potential energy surface were expected to yield improved accuracy for the collision rates. However, as explained by Wernli et al. (2007b), problems in the numerical realization resulted in the results for ortho- $\text{H}_2$  being invalid, while those for para- $\text{H}_2$  are thought to be satisfactory.

Quantum calculations by Faure and Wiesenfeld (2011) of collisions between ortho- $\text{H}_2$  and  $\text{HC}_3\text{N}$  have recently been made available to us. Collisions with para- $\text{H}_2$  show a propensity for  $\Delta J = 2$  collisions, but the rates are only modestly smaller for  $\Delta J = 1$  and  $\Delta J = 3$ . The new rates for collisions with ortho- $\text{H}_2$  are quite different, favoring  $\Delta J = 1$ . The result is that while the largest ortho- $\text{H}_2$  rates are up to a factor of 4 larger than the para- $\text{H}_2$  rates, the overall collision rates are more nearly equal. Both the ortho- $\text{H}_2$  and para- $\text{H}_2$  rates are modestly larger than the Green and Chapman rates, even when the latter are scaled by a factor 1.39 to account for the lower reduced mass of  $\text{H}_2$  compared to that of He.

We have used the RADEX code (Van der Tak et al. 2007) to calculate the statistical equilibrium level populations and resulting line intensities from a molecular cloud. We adopt a column density  $N(\text{HC}_3\text{N}) = 10^{12} \text{ cm}^{-2}$  and a line width of 1 km/s, which ensures that all transitions are optically thin, and which is close to  $N(\text{HC}_3\text{N})$  determined for the B213 filament, in what follows. In Fig. 7 we show the ratio of the intensity of the  $J = 10-9$  to that of the  $J = 2-1$  transition as a function of molecular hydrogen density, for a kinetic temperature of 10 K. For optically thin emission and equal line widths (as found in the present data), the ratios of peak and integrated temperatures are the same. As seen in Fig. 7, the line ratio reaches specified value for a lower density of ortho- $\text{H}_2$  than of para- $\text{H}_2$ . The difference, however, is only about a factor of 1.3 to 1.5 in density.

The ortho to para  $\text{H}_2$  ratio (OPR) is quite uncertain. If the molecular hydrogen is formed with its internal levels populated at a temperature comparable to the molecule's binding energy, the OPR should just reflect the relative statistical weights of the two spin modifications, since their energy difference is so small in comparison. This

would result in an OPR equal to 3. On the other hand, equilibration at the cloud temperature should result in a ratio determined by the  $J=1$  to  $J=0$  energy difference. Since this is equivalent to 171 K, the result is an OPR close to zero for a dark cloud kinetic temperature of 10 K – 15 K. Observational results are difficult to obtain, and are mixed, but suggest that an OPR  $\simeq 1$  is a reasonable upper limit even in moderately warm regions (Neufeld, Melnick & Harwit 1998). This may be a reflection of timescales for interconversion of the spin modifications.

Due to the very modest difference between the ortho and para collision rates, even though one might have to consider OPR between 0 and 1, the excitation of  $\text{HC}_3\text{N}$  is only very weakly dependent on this poorly-known quantity. In dark clouds there is evidence for enhanced molecular deuteration, which requires very low ortho  $\text{H}_2$  abundance (Flower, Pineau Des Forêts & Walmsley 2006). Given the above considerations, we will adopt the para- $\text{H}_2$  rates (i.e. an OPR = 0) for obtaining densities in the B213 filament.

Our imprecise knowledge of the kinetic temperature results in an additional uncertainty.  $^{12}\text{CO}$  data suggests a kinetic temperature between 12 K and 15 K, but this may apply more to the outer portion of the filament, since the lower transitions of this species are very optically thick and do not really sample the interior of the filament. It is reasonable that the inner portions in a region such as this with a  $\text{H}_2$  column density corresponding to  $\simeq 10$  mag of visual extinction will be significantly cooler (Evans et al. 2001; Shirley et al. 2005). Thus, for the optically thin  $\text{HC}_3\text{N}$  emission, a kinetic temperature of 10 K seems appropriate. In Fig. 8 we show the effect of changing the kinetic temperature from 10 K to 15 K. The hydrogen density inferred for a given observed ratio is lower for the higher temperature, but in the range of values observed ( $\leq 0.5$ ), the density difference does not exceed a factor of 2.

Other than the uncertainty in the knowledge of collision rates, the uncertainty in the derived density is dominated by the uncertainty in the derived optical depth for the  $J=2-1$  transition. The uncertainty in the fitted optical depth is affected by both the RMS noise, which is 0.09 K and 0.03 K per channel for TMC1C and B213, respectively, and the line strength. For TMC1C, the sigma for the derived optical depth of the main hyperfine component is 0.23 compared to its best fit value 0.47. This corresponds to a one sigma range of  $J=2-1$  corrected integrated intensities between 2.3 K km/s and 3.0 K km/s. The RMS for the fitted integrated intensities of the  $J=10-9$  transition is considerably smaller, about 3%. The range of line ratios for TMC1C is thus between 0.17 and 0.13. The resulting uncertainty in density would also depend on the shape of the excitation curve (Fig. 7). The one sigma range of derived densities for TMC1C are  $1.25 \times 10^4 \text{ cm}^{-3}$  to  $1.04 \times 10^4 \text{ cm}^{-3}$ , which corresponds to about a 20% relative uncertainty for the derived density for TMC1C. For the B213 positions, the statistical uncertainties for derived optical depth are generally on the same order as the value of optical depth itself. For position A, the range of derived densities is  $1.9 \times 10^4 \text{ cm}^{-3}$  to  $2.9 \times 10^4 \text{ cm}^{-3}$ , which corresponds to about a  $\pm 20\%$  uncertainty. This is representative of the statistical uncertainty in the density determined for B213.

In summary, the largest source of uncertainty in the de-

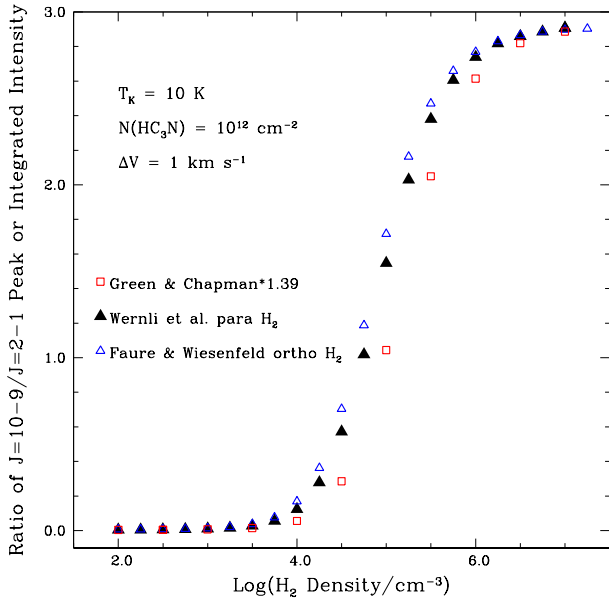


FIG. 7.— Dependence of the ratio of HC<sub>3</sub>N J = 10-9 to J = 2-1 intensities as a function of H<sub>2</sub> density. The molecular column density is chosen so that all transitions are optically thin; in this case the ratios for the peak and the integrated temperatures are the same. The three sets of points correspond to the Green & Chapman (1978) rates, the Wernli et al. (2007a) rates for para-H<sub>2</sub>, and the Faure & Wiesenfeld (2011) rates for ortho-H<sub>2</sub>. The observed antenna temperature ratio of 0.4 corresponds to a H<sub>2</sub> density  $\simeq 10^4$  cm<sup>-3</sup>.

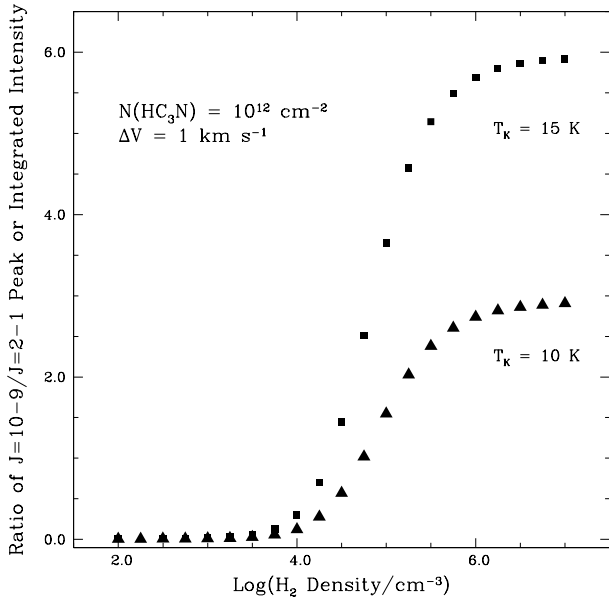


FIG. 8.— Ratio of HC<sub>3</sub>N J = 10-9 to J = 2-1 transition as a function of the H<sub>2</sub> density, for kinetic temperatures of 10 K and 15 K. The collision rates used are those of Wernli et al. (2007a) for para-H<sub>2</sub> (J = 0). The reduction in the derived density that results when the observed intensity ratio is less than 0.5 is relatively small, less than a factor of 2, in changing the kinetic temperature from 10 K to 15 K.

rived density arises from the imprecisely known kinetic temperature, followed by the uncertainty in the H<sub>2</sub> ortho to para ratio. The uncertainty caused by noise in the line measurement is in the range 20 to 40 percent. Given the reasonable assumptions that have been made for each of the items as discussed above, we feel that

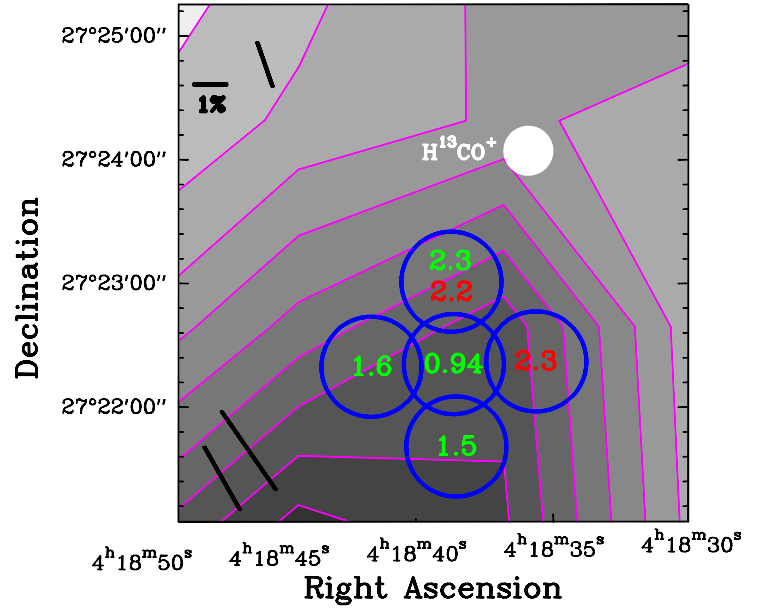


FIG. 9.— The measured volume densities for the 5.6 km/s (in green) and 6.7 km/s (in red) components at positions A through E in the B213 Taurus filament (Table 1), for a kinetic temperature of 10 K and OPR = 0 (see text for discussion). The units of the density are 10<sup>4</sup> cm<sup>-3</sup>. The blue circles reflect the GBT beam size. The peak of H<sup>13</sup>CO<sup>+</sup> emission is indicated by the white circle, with diameter reflecting the beam size of the Nobeyama telescope and center corresponding to core 10b listed in Table 1 of Onishi et al. (2002). The dark vectors denote the orientation of the magnetic field based on optical absorption measurements (Chapman et al. 2011). The underlying image is as in Fig. 4

we have a determination of the volume density through the measurements of HC<sub>3</sub>N line ratio that is accurate to within a factor of  $\pm 50\%$  (factor of three).

The density we derive (next to last column of Table 2) for TMC1C is about  $1.1 \times 10^4$  cm<sup>-3</sup>. For B213, the derived densities are a factor of 1.4 to 2 higher due to the larger observed line ratio, except for position E, which has slightly lower density than TMC1C. The derived densities for the five spatial positions are indicated in Fig. 9.

We also derive the column density of HC<sub>3</sub>N using the observed intensity and the excitation conditions derived above. For an optically thin transition, the column density of the upper level is simply proportional to its integrated intensity

$$N_u = \frac{8\pi k\nu^2}{hc^3 A_{ul}} \int T_{mb} dv, \quad (1)$$

where  $T_{mb}$  is the main beam antenna temperature as described in the data section. We use the integrated intensities of the optically thin J=10-9 transition to obtain  $N(J=10)$ . To obtain the total column density of HC<sub>3</sub>N, we utilize the level populations provided by the same Radex calculations that produced Fig. 7 for collisions with ortho-H<sub>2</sub>. The resulting column densities are listed in the last column of Table 2. The HC<sub>3</sub>N column density of B213 is within a factor of two of 10<sup>12</sup> cm<sup>-2</sup>, while that of TMC1C is one order of magnitude higher. This is consistent with the well-known fact that carbon chain molecules have significantly enhanced abundance in TMC1C.

## 5. DISCUSSION: THE 3D STRUCTURE OF B213

The volume density measurements enable us to examine the 3D structure of the B213 filament. We first consider the 2D dimension of the B213 filament projected on the sky. At the distance of Taurus, one minute of arc corresponds to about 0.04 pc. The shorter dimension of the B213 filament in the neighborhood of position A is about 4 arcminutes or 0.16 pc as seen in 2MASS extinction. The filament is elongated by a factor of at least 10 in the orthogonal direction.

The median 2MASS extinction for these positions is about 6.3 mag, which corresponds to  $N(\text{H}_2) = 6 \times 10^{21} \text{ cm}^{-2}$ . This is close to that found from  $^{13}\text{CO}$  (Pineda et al. 2010) assuming  $X(\text{CO}) = 2 \times 10^{-4}$ , indicating that there is relatively little depletion of CO, which if present would imply an excessively large total column density. The modest depletion is consistent with the density we derive and a depletion time scale of a few  $\times 10^5$  yr (Bergin & Tafalla 2007; Pineda et al. 2010), if the filament age is not much more than that. The average density found from our  $\text{HC}_3\text{N}$  observations is about  $(1.8 \pm 0.7) \times 10^4 \text{ cm}^{-3}$ . From the column density and the volume density, the line of sight dimension is found to be 0.12 pc, which is comparable to the shorter dimension of the filament projected on the sky. The derived line of sight dimension is one order of magnitude shorter than the filament's elongated dimension in the plane of the sky, which effectively rules out B213 being an edge-on sheet.

As shown in Fig. 4, we detected the higher rotational transition ( $J=10-9$ ) of  $\text{HC}_3\text{N}$  in 14 spatial positions, which are distributed contiguously along the filament. Detection of the lower transition was limited in only 5 spatial positions not because of insufficient excitation, but due to the difficulty of detecting the multiply hyperfine-split  $J = 2-1$  transition. Fig. 9 shows density measurements at 5 spatial positions. The two velocity components present in these positions yield very similar densities. All measured densities are within a factor of 2.5 of each other over a projected separation of approximately 0.1 pc. The line widths at all observed positions are small and their peak velocities are similar. The volume density measured for these two velocity components cannot result from an isolated "dense core" only seen high density tracers such as  $\text{H}^{13}\text{CO}^+$ . These densities are also unlikely to be the result of only a few very dense cores much smaller than the beam and resulting beam dilution of their emission. We seem to be probing lines of sight representative of the B213 filament as a whole. We cannot, however, rule out completely a highly clumpy cloud structure consisting of a large number of very small dense clumps and an extended low density component. Evaluating such substantially more complex structures will require observations at much higher spatial resolution.

If B213 is indeed a self-gravitating cylinder, an extended low density 'halo' resulting simply from the requirement of hydrostatic equilibrium should be present. Chandrasekhar & Fermi (1953), Larson (1985), Inutsuka & Miyama (1992) and others have studied the configuration and evolution of infinite isothermal self-gravitating cylinders. The radial density profile of such cylinder turns out to be of the Plummer type for both the stable and collapsing case with a 'flat' (approximately uni-

form density) central part and a halo characterized by an effectively rapidly-dropping power-law density  $n \sim (1/r)^4$  (see Eq. 1 in Inutsuka & Miyama 1992). In such cases, the density measured by  $\text{HC}_3\text{N}$  will probe only the central 'flat' part, as the 'halo' cannot excite the higher rotational transitions. The dimension thus derived cannot rule out the existence of the extended low density halo, but will characterize the central core of the filament, which could be considered to represent the radial size of the filament.

Cylindrical, i.e. filamentary, structures are of increasing interest at the present time due to their prevalence in recent surveys of the ISM, e.g. Goldsmith et al. (2008), André et al. (2010), and Molinari et al. (2010). The filaments found in these surveys differ by orders of magnitude in terms of physical length, mass, and their star formation content. These results show that, at least in 2D projection, elongated structures are a common feature of the interstellar medium. Filaments can be produced in numerical simulations of vastly different physical conditions. Filaments show up in a strongly magnetized (sub-Alfvénic) MHD simulation with ambipolar diffusion (Li et al. 2012). Filaments are also seen in simulation of supersonic converging flows without magnetic field (Gong & Ostriker 2011). Filamentary structures are not restricted to fluid simulations (with or without magnetic field, with or without dominant turbulence); filamentary structures are prevalent in cold dark matter cosmological simulations (Springel et al. 2005), where the most important physics are gravity and structure growth.

To determine the driving factor of structure formation in the star-forming ISM, the measurement of physical parameters in addition to morphology is critical. The data presented here are a limited first step. One particular relevant regime of ISM evolution is molecular cloud formation induced by colliding HI streams (Ballesteros-Paredes et al. 1999). A flattened structure (sheet) is expected at the shock front (Vázquez-Semadeni et al. 2006). The subsequent structure growth depends on the relative importance of different unstable modes, which in turn depend on the physical conditions. In an illustrative discussion by Heitsch et al. (2005), the structures that become visible largely reflect the ratio between volume density and converging velocity. When the density is high, thermal instability dominates and the dense structures that grow tend to be contained near the shock front, maintaining a filamentary appearance. When the ratio of density to colliding velocity decreases, Kelvin-Helmholtz and nonlinear thin sheet instabilities grow faster and tend to produce structures perpendicular to the elongation of the shock front.

We are not yet at a stage to differentiate among different simulations, for which the methods themselves are evolving rapidly. It is, however, tantalizing to describe the evolution of ISM leading to star formation as the following sequence: sheet  $\rightarrow$  filament  $\rightarrow$  cores. A flattened structure (sheet) can be produced by colliding streams or other shocks as discussed above. A self-gravitating sheet will preferentially fragment into filaments (Miyama, Narita & Hayashi 1987). Inutsuka and Miyama (1992) carried out self-similar calculation of isothermal cylinder and derived a critical filament "line mass", consistent with that in Ostriker (1964), beyond which the filament is expected to fragment and collapse

into cores. This last stage of filament-to-cores evolution seems to be emerging as a phenomenon often found in recent observational studies, such as Hacar & Tafalla (2011) and Schmalzl et al. (2010).

In observing multiple transitions of HC<sub>3</sub>N toward Taurus filaments, we do not see any suggestions of a sheet extended along the line of sight. If a sheet had been present, it must have already evolved or dissipated. The line width and velocity gradient of HC<sub>3</sub>N gas are both small at around 0.3 km/s. At the  $\sim 10$  K temperature of gas in the filament, this is marginally supersonic. For a sound speed of 0.127 km/s corresponding to a line width of 0.3 km/s FWHM, the critical line mass is about 7.6 M<sub>⊙</sub>/pc. For B213, this corresponds to a column density of  $N(\text{H}_2) = 4 \times 10^{21} \text{ cm}^{-2}$ , somewhat smaller than the observed value, suggesting that B213 is susceptible to collapse/fragmentation to produce cores.

The line width of HC<sub>3</sub>N in B213 filament is similar to that of 180 in L1517 (Hacar & Tafalla 2011), while larger than that of N<sub>2</sub>H<sup>+</sup> that is observed in the same study. Hacar & Tafalla also found a subsonic velocity difference among N<sub>2</sub>H<sup>+</sup> cores contained in the L1517 filaments and were able to fit the radial profiles of 180 emission using isothermal cylinders. These authors postulate a two step core formation processes including, first, a subsonic filament, and second, fragmentation-produced cores. The measured volume density and line of sight dimension of B213 are consistent with it being a cylinder-like ‘true’ filament in which HC<sub>3</sub>N traces the gas in a manner similar to 180 in L1517. The internal motions of the B213 filament are still slightly supersonic, which could mean that B213 is at an earlier evolutionary stage than L1517, having yet to go through the stage in which the line width drops and core formation begins.

The volume density measurements and the velocity information presented in this paper will be of additional value when radiative transfer is added to various simulations and modeled spectral line profiles can be compared

directly with those observed. The density measurements in this study fit into a developing picture of molecular cloud evolution from turbulent gas to coherent filaments to subsonic cores.

## 6. CONCLUSIONS

We have determined the volume H<sub>2</sub> densities along five lines of sight (which include a total 6 distinct components) in a prominent filament in Taurus, B213, to be on average  $(1.8 \pm 0.7) \times 10^4 \text{ cm}^{-3}$ . The density determinations are based on excitation calculations that fit the line ratio between HC<sub>3</sub>N 10-9 and HC<sub>3</sub>N 2-1 transitions. The clearly-resolved hyperfine components of the 2-1 transition enable us to determine the peak opacity of the 2-1 line to be smaller than 1.3. The line of sight dimension of the dense portion of B213 filament is  $\simeq 0.25$  pc, comparable to the smaller plane-of-the-sky dimension of the filament, which is about 0.16 pc. These dimensions are both much smaller than the longer dimension of B213, which is a few pc. The FWHM line width of HC<sub>3</sub>N is about 0.3 km/s, which is slightly supersonic. We conclude that B213 is likely a true filament, but that it has not yet formed dense cores throughout.

This work has been partly supported by China Ministry of Science and Technology under State Key Development Program for Basic Research (2012CB821800). We thank the staffs at the Green Bank Telescope and the Arizona Radio Observatory for their support during these observations. We also appreciate very helpful discussions with Steve Stahler on molecular cloud evolution. We acknowledge valuable input from Hao Gong and Pak-Shing Li regarding numerical simulations. We thank Laurent Wiesenfeld for communicating his most recent calculations of HC<sub>3</sub>N collisional excitation rates. This research was carried out in part at the Jet Propulsion Laboratory, California Institute of Technology which is supported by the National Aeronautics and Space Administration.

## REFERENCES

- André, P., Men’shchikov, A., Bontemps, S., et al. 2010, *A&A*, 518, L102
- Arzoumanian, D., et al. 2011, *A&A*, 529, L6
- Avery, L. W., MacLeod, J. M., & Broten, N. W. 1982, *ApJ*, 254, 116
- Ballesteros-Paredes, J., Hartmann, L., & Vázquez-Semadeni, E. 1999, *ApJ*, 527, 285
- Bergin, E.A. & Tafalla, M. 2007, *ARA&A*, 45, 339
- Chandrasekhar, S., & Fermi, E. 1953, *ApJ*, 118, 116
- Chapman, N. L., Goldsmith, P. F., Pineda, J. L., Clemens, D. P., Li, D., & Krčo, M. 2011, *ApJ*, 741, 21
- Evans, N. J. II, Rawlings, J. M., Shirley, Y. L., & Mundy, L. G. 2001, *ApJ*, 557, 193
- Faure, A. & Wiesenfeld, L. 2011, private communication
- Flower, D. R., Pineau Des Forêts, G., & Walmsley, C. M. 2006, *A&A*, 449, 621
- Goldsmith, P. F., Heyer, M., Narayanan, G., Snell, R., Li, D., & Brunt, C. 2008, *ApJ*, 680, 428
- Gong, H., & Ostriker, E. C. 2011, *ApJ*, 729, 120
- Green, S. & Chapman, S. 1978, *ApJS*, 37, 169
- Hacar, A., & Tafalla, M. 2011, *A&A*, 533, A34
- Heitsch, F., Burkert, A., Hartmann, L. W., Slyz, A. D., & Devriendt, J. E. G. 2005, *ApJ*, 633, L113
- Inutsuka, S.-I., & Miyama, S. M. 1992, *ApJ*, 388, 392
- Larson, R. B. 1985, *MNRAS*, 214, 379
- Li, P. S., McKee, C. F., & Klein, R. I. 2012, *ApJ*, 744, 73
- Lin, C. C., Mestel, L., & Shu, F. H. 1965, *ApJ*, 142, 1431
- McKee, C. F., & Ostriker, E. C. 2007, *ARA&A*, 45, 565
- Men’shchikov, A., et al. 2010, *A&A*, 518, L103
- Molinari, S., Swinyard, B., Bally, J., et al. 2010, *A&A*, 518, L100
- Miyama, S. M., Narita, S., & Hayashi, C. 1987, *Progress of Theoretical Physics*, 78, 1273
- Narayanan, G., Heyer, M. H., Brunt, C., Goldsmith, P.F., Snell, R., Li, D. 2008, *ApJS*, 177, 341
- Neufeld, D.A., Melnick, G.J., & Harwit, M. 1998, *ApJ*, 506, L75
- Onishi, T., Mizuno, A., Kawamura, A., Tachihara, K., & Fukui, Y. 2002, *ApJ*, 575, 950
- Ostriker, J. 1964, *ApJ*, 140, 1056
- Pineda, J.L., Goldsmith, P.F., Chapman, N., Snell, R.L., Li, D., Cambrésy, L., & Brunt, C. 2010, *ApJ*, 721, 686
- Pratap, P., Dickens, J. E., Snell, R. L., et al. 1997, *ApJ*, 486, 862
- Rebull, L. M., et al. 2010, *ApJS*, 186, 259
- Schloerb, F. P., Snell, R. L., & Young, J. S. 1983, *ApJ*, 267, 163
- Schmalzl, M., Kainulainen, J., Quanz, S. P., et al. 2010, *ApJ*, 725, 1327
- Schneider, S. & Elmegreen, B. E. 1979, *ApJS*, 41, 87
- Sheffer, Y., Rogers, M., Ferman, S. R., et al. 2008, *ApJ*, 687, 1075
- Shirley, Y. L., Nordhaus, M. K., Grcevich, J. M., Evans, N. J. II, & Rawlings, J. M. C. 2005, *ApJ*, 632, 982
- Springel, V., White, S. D. M., Jenkins, A., et al. 2005, *Nature*, 435, 629
- Stepnik, B., et al. 2003, *A&A*, 398, 551
- van der Tak, F. F. S., Black, J. H., Schöier, F. L., Jansen, D. J., & van Dishoeck, E. F. 2007, *A&A*, 468, 627
- Vázquez-Semadeni, E., Ryu, D., Passot, T., González, R. F., & Gazol, A. 2006, *ApJ*, 643, 245
- Wernli, M., Wiesenfeld, L., Faure, A., & Valiron, P. 2007, *A&A*, 464, 1147 (2007a)
- Wernli, M., Wiesenfeld, L., Faure, A., & Valiron, P. 2007, *A&A*, 475, 391 (2007b)



TABLE 2  
FITTED HC<sub>3</sub>N LINE CHARACTERISTICS

Source	Comp.	HC <sub>3</sub> N 2-1					HC <sub>3</sub> N 10-9					Line Ratio	n(H <sub>2</sub> )	N(HC <sub>3</sub> N)
		V <sub>0</sub>	FWHM	T <sub>main</sub>	$\int T dv$	$\tau_{main}$	V <sub>0</sub>	FWHM	T <sub>main</sub>	$\int T dv$	$\frac{\int T(10-9)dv}{\int T(2-1)dv}$			
		km/s	km/s	K	K km/s		km/s	km/s	K	K km/s		10 <sup>4</sup> cm <sup>3</sup>	10 <sup>12</sup> cm <sup>-2</sup>	
TMC1C	s	5.4	0.21	5.34	2.6	0.47	5.2	0.29	1.23	0.37	0.15	1.1	18.	
B213 A	b	5.7	0.14	0.45	0.15	0.48	5.6	0.28	0.20	0.058	0.39	2.3	1.5	
B213 A	r	6.8	0.17	0.22	0.083	0.00	6.7	0.18	0.16	0.030	0.36	2.2	0.80	
B213 B	b	5.7	0.14	0.14	0.046	0.00	NA	NA	NA	NA	NA	NA	NA	
B213 B	r	6.8	0.17	0.20	0.076	0.00	6.7	0.19	0.14	0.029	0.38	2.3	0.74	
B213 C	s	5.6	0.17	0.37	0.14	0.27	5.5	0.29	0.10	0.031	0.22	1.5	1.1	
B213 D	s	5.6	0.19	0.24	0.10	0.14	5.5	0.19	0.12	0.024	0.23	1.6	0.85	
B213 E	s	5.6	0.17	1.03	0.39	1.30	5.5	0.18	0.19	0.038	0.097	0.94	1.9	

NOTE. — The units for the fitted FWHM linewidth and central velocity V<sub>0</sub> are km/s. The units for T<sub>main</sub>, the main beam antenna temperature from the fitting procedures described in the text, are Kelvin. In the second column, s denotes a single velocity component, b and r denote blue and red velocity components, respectively. Column 7 gives the peak optical depth of the F=3-2 (main) HFS component of the J=2-1 transition. The integrated main beam temperatures having units of K km/s have been corrected for the optical depth where appropriate. An optical depth of zero indicates an optically thin line. "NA" indicates a nondetection.